ACS Photonics

Article

pubs.acs.org/journal/apchd5

Ultra Sensing by Combining Extraordinary Optical Transmission with Perfect Absorption

Thomas G. Mayerhöfer,*[,†] Richard Knipper,[†,‡] Uwe Hübner,[†] Dana Cialla-May,[†,‡] Karina Weber,[†,‡] Hans-Georg Meyer,[†] and Jürgen Popp[†,‡]

[†]Leibniz Institute of Photonic Technology (IPHT), Albert-Einstein-Str. 9, D-07745 Jena, Germany

[‡]Institute of Physical Chemistry and Abbe Center of Photonics, Friedrich Schiller University, Helmholtzweg 4, Jena, D-07743, Germany

Supporting Information

ABSTRACT: Extraordinary optical transmission and perfect absorption are two plasmonic-based optical phenomenona that are both accompanied by high local field enhancements that can be exploited for biological and chemical sensing. Here we merge both phenomenona in a slit array metamaterial perfect absorber consisting of a dielectric layer sandwiched between two metallic layers of which the upper layer is perforated with a periodic array of slits. Period and dimensions of the slits and thickness of the dielectric layer are tuned in a way that virtually all light of a certain wavelength incident on the surface passes through the slits and is subsequently absorbed. As a consequence, light−matter interaction is greatly enhanced in the slits. Thus, already small concentrations of analytes down to a monolayer attached to the sidewalls of the slits can be detected by refractive index sensing and identified by their spectral fingerprints with a standard mid-infrared lab spectrometer.

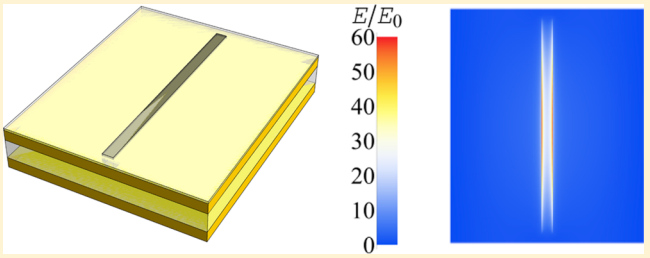

KEYWORDS: *plasmonics, metamaterials, sensing, surface enhanced infrared spectroscopy, extraordinary optical transmission, perfect absorption*

A metamaterial perfect absorber (MPA) is a subwavelength structured device in which all incident radiation is absorbed at a particular wavelength.[1] As a consequence, at this wavelength transmission and reflection are zero. In practice, zero transmission is made possible by a highly reflecting layer of a coinage metal, for example gold, with a sufficient thickness so that virtually no radiation can pass through. Absorption is usually caused by the excitation of a surface plasmon polariton (SPP). Since light cannot couple to a smooth metallic surface, it is the task of a proper surface structure to enable the excitation of an SPP at the desired wavelength. Usually this surface structure consists of metallic particles on a thin dielectric film to separate the particles from the basic metal layer. These metallic particles can have a variety of forms like, in the simplest cases, cylinders[2] or rectangular parallelepipeds,[3−7] crosses,[8,9] and more complicated forms like trapezoids and so on.[10−12] The design of such metamaterial perfect absorbers was partially driven by the effort to avoid interactions between the individual particles and unit cells. In a few cases, however, the opposite design strategy was selected, that is, using a subwavelength hole array (SHA) instead of metallic particles as the surface structure.[13,14] These structures are of particular interest also from a theoretical point of view, since perfect absorption at one wavelength would mean that all light shining on the MPA has to pass through the holes in order to be absorbed by the structure if the perforated metal layer is thick enough to block direct transmission. In refs 13 and 14, however, a hole array layer is used that is optically thin at the resonance wavelength of the MPA, so that part of the light is transmitted directly through the metal layer. From an application oriented point of view, the SHA-MPA combination has very attractive features for both chemical and biological sensors. Compared to SHAs, the SHA-MPA combination can be expected to lead to much higher field enhancements within the holes, the "hot spots". Further, compared to particle-based MPAs, with SHA-MPA it proves much easier to concentrate the analyte in these volumes of the highest field enhancements. If the resonance wavelengths of the SHA-MPA combination is tuned for the absorption at mid-infrared (MIR) frequencies, from the presence of the analyte not only will a band shift ensue due to the different dielectric environment of the gold surface,[2] but also chemical information will be provided by the enhancement of the spectral footprint of the analyte. This has already been shown for either SHAs with enhanced transmission[15] or nanoantennas[16−18] with plasmonic excitations in the MIR.

It was the goal of the present work to design and manufacture exactly this sort of SHA-MPA combination for the MIR spectral region. The structures we fabricated were then tested with the model analyte octadecanethiol and, additionally,

Received: June 10, 2015
Published: October 21, 2015

DOI: 10.1021/acsphotonics.5b00321
ACS Photonics 2015, 2, 1567−1575

with DNA. We believe that the SHA-MPA combination proves to be a promising candidate to serve as an integral component of a future application for ultrasensitive biological and chemical detection and quantification.

The basic structure of one elementary cell of the SHA-MPA is depicted in Figure 1. A 50 nm gold film serves as the first layer (the base). As gold films tend to grow in a columnar way with increasing thickness, causing poor thickness homogeneity, we decided to employ a base layer as thin as possible. Based on the optical constants of gold[19] we calculated that a 50 nm gold film would exhibit a transmission of less than 1×10^{-3} for wavelengths larger than 2.26 μm, which is small enough for our goal to additionally enhance the electric field within the slits. On top of the 50 nm gold base layer, the dielectric layer was placed, for which we decided to use Al_2O_3, and not SiO_2. Not only is the onset of the Reststrahlenband of Al_2O_3 shifted to a higher wavelength than with SiO_2,[20] which in general allows for the building of an infrared active substrate down to about 10 μm (1000 cm^{-1}). Therefore, the resonance wavelength of the substrate will be tunable over most of the IR spectral range that is interesting for biological molecules. Furthermore, as will be shown later, the enhancement will be concentrated on the slit walls and not on the gold base layer. Employing Al_2O_3 as the dielectric, the slit will not penetrate the dielectric layer down to the base due to the very small Ar^+-ion beam etching rate of Al_2O_3. As a consequence, only the side walls of the slit will be able to be functionalized. On top of the dielectric, the thickness $t_{Al_2O_3}$ of which is in the range of 90 nm, a second 50 nm thick gold layer is placed. To prevent the surface layer from being functionalized, we applied a 10 nm thick layer of SiO_2 onto the second gold layer. This SiO_2 layer completes the layer stack. With a period a in the y-direction and b in the x-direction (see Figure 1b), slits with a length c (along y) and width d (along x) are then etched out.

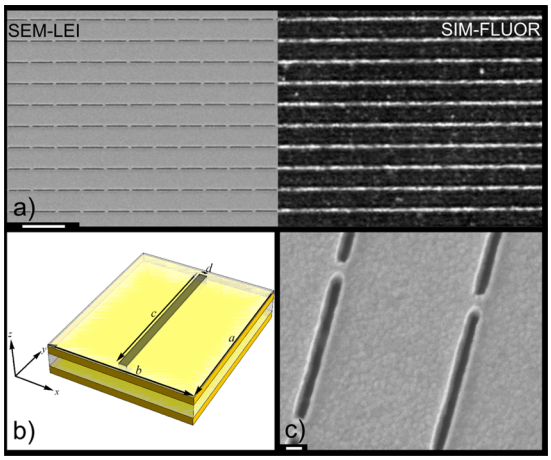

Figure 1. Structure of the subwavelength slit array metamaterial perfect absorber. (a) Combined SEM and SIM-FLUOR image (scale bar 2 μm). (b) Unit cell of the slit metamaterial perfect absorber. The layer stack of the fundamental structure consists of a 50 nm thick gold base layer followed by an Al_2O_3 layer and a second 50 nm thick gold layer (metal−insulator−metal layer stack). The top SiO_2 layer (thickness: 10 nm) serves to inhibit functionalization. The period in the y-direction of the unit cell is a, the one in the x-direction b. c is the slit length and d is the slit width, respectively. The depth of the slit is 60 nm so that the base level coincides with the surface of the Al_2O_3 layer. (c) Tilted SEM micrograph (scale bar 100 nm; pitch b, 910 nm; pitch a, 1100 nm; slit width d, 45 nm; slit length c, 1005 nm; $t_{Al_2O_3}$ = 90 nm; grating size, 1 × 1 mm^2).

As a consequence of the design, the analyte can only be found in the region of the slits, which we could prove with help of high-resolution structured illumination fluorescence imaging (Figure 1a, right).

The original idea of this design was that for small widths d of the slits extraordinary high enhancement factors for the electric fields would follow. Indeed this proved to be the case, yet, as will be shown, only for very small slit widths d < 20 nm which are, at the moment, difficult to realize from the technological point of view. Nevertheless, even for d = 50 nm considerable enhancement factors result at the resonance wavenumbers, which can be explained by the fact that, with perfect absorption (A = 1), all the light has to pass through the slit. At the same time, the slit generates highly anisotropic optical properties. While the slit substrates show near perfect absorption in the infrared spectral range for x-polarized radiation, the substrates cannot be optically distinguished from an unstructured, thick gold layer for y-polarized radiation.

This is demonstrated by a numerical simulation employing the finite difference time domain (FDTD)method for a substrate with $t_{Al_2O_3}$ = 90 nm, a = 1100 nm, b = 910 nm, c = 1000 nm, and d = 50 nm in Figure 2.

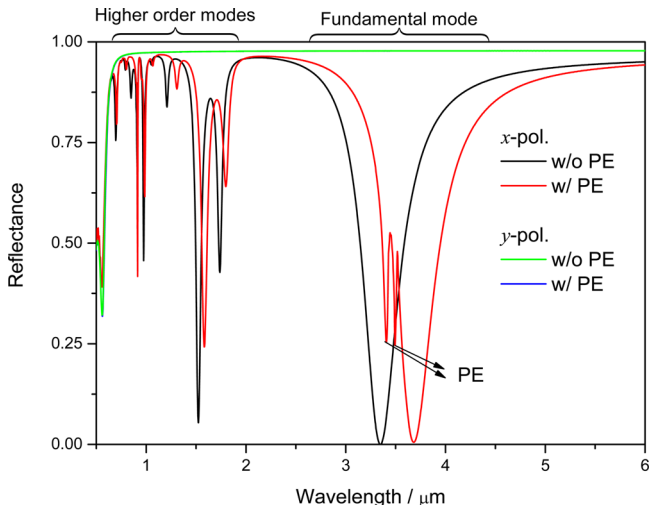

Figure 2. Simulated spectra of a subwavelength slit array metamaterial perfect absorber. Simulated reflectance spectra of a slit MPA with a = 910 nm, b = 1100 nm, c = 1000 nm, d = 50 nm, and $t_{Al_2O_3}$ = 90 nm for normal incidence. The figure compares the x-polarized spectra of the slit MPA with an empty slit (black) and a slit filled with PE (red). The y-polarized spectrum (green/blue) does not vary with the slit content and is essentially that of an (unstructured) gold surface.

Since reflection spectroscopy requires recording a reference spectrum (in the IR spectral range often a gold mirror is used) for future application it might be possible to use a y-polarized spectrum of the substrate as this reference. (For the measurements shown below, however, a gold mirror served as reference.)

For the slit array perfect absorber we aim at a resonance around 3000 cm^{-1} in order to selectively enhance the C−H valence vibrations present in nearly all organic and biologic molecules which are located in this spectral range. According to our simulations the substrate with $t_{Al_2O_3}$ = 90 nm, a = 1100 nm,

DOI: 10.1021/acsphotonics.5b00321
ACS Photonics 2015, 2, 1567−1575

b = 910 nm, c = 1000 nm, and d = 50 nm has exactly such a resonance with less than 0.01% reflectance R, meaning that the absorption A is higher than 99.94% (since $A + R + T = 1$ and the transmittance of the base layer $T < 5 \times 10^{-4}$ at the resonance wavelength). In addition, the perfect absorber design leads to a very narrow absorption line with a full width at half-maximum (fwhm) of about 0.45 μm. When the slit is loaded completely with PE, the simulation result changes in two ways (cf. Figure 2). First, we notice a shift of all resonances, including most of the higher order plasmon modes which populate the region below 2 μm, to higher wavelengths, and second, we see a change of the band shape of the main resonance.

The resonance shift is a consequence of the changed dielectric properties of the medium in the slit.

The change in the band shape of the main resonance is due to the interaction of the SPP with the C−H vibrations of the PE. For PE, we expect two different C−H stretching vibrations, the asymmetric C−H stretching vibration $\nu_{as}(CH_2)$ at 3.427 μm (2918 cm^{-1}) and the symmetric C−H stretching vibration $\nu_{s}(CH_2)$ at 3.503 μm (2853 cm^{-1}). Inspecting the corresponding spectrum in Figure 2, we indeed find two additional bands, the minima of which are, however, slightly shifted to 3.406 and 3.494 μm. The reason for this shift can be found in the Fano-type interaction between the comparably broad band absorption caused by the SPP and the narrow band resonances of the PE. When the wavelength of the plasmonic mode is shifted relative to the vibrational modes, the PE bands transform from electromagnetically induced absorption (EIA) to electromagnetically induced transparency (EIT). The latter occurs when the resonance frequencies of plasmon and vibration coincide. Since the medium in the slit and, with it, the index of refraction changes (the average index of refraction increases with the filling ratio), the SPP is shifted to a longer wavelength. As a consequence, the difference between the resonance frequencies of PE and SPP increases, resulting in a state in between EIA and EIT. This effect will be discussed in more detail later. In general, we can tune the resonance by varying the period in x-direction, the thickness of the Al_2O_3-layer $t_{Al_2O_3}$ and the slit width. (N.B.: Altering the layer thickness of the structured gold layer would also have an influence, in particular, if decreased. However, since we want to make sure that direct transmission through this layer remains virtually zero, we did not vary the thickness of the gold layer.)

The dependence of the SPP wavelength on the slit parameters is demonstrated in Figure 3. Accordingly the reduction of the slit width from 70 to 10 nm leads to a shift of the resonance from about 3.25 μm up to 4.27 μm. For slit widths lower than 30 nm, however, the reflectance increases from 1% to about 15% for 10 nm slit width. A lower change of the resonance wavelength can be achieved by varying the period in x-direction between 820 and 1000 nm. For a = 820 nm, the resonance wavelength is 3.18 μm, which increases to 3.51 μm for a = 1000 nm. In contrast to the variation of the resonance wavelengths due to changing the slit width, the reflectance stays for the period range considered below 1%. Even less variation of the resonance wavenumber is achieved due to a variation of the thickness of the Al_2O_3 layer $t_{Al_2O_3}$. For $t_{Al_2O_3}$ = 60 nm the resonance can be found at 3.47 μm, which decreases with increasing $t_{Al_2O_3}$. Accordingly, we find for $t_{Al_2O_3}$ = 120 nm, the resonance is at 3.32 μm.

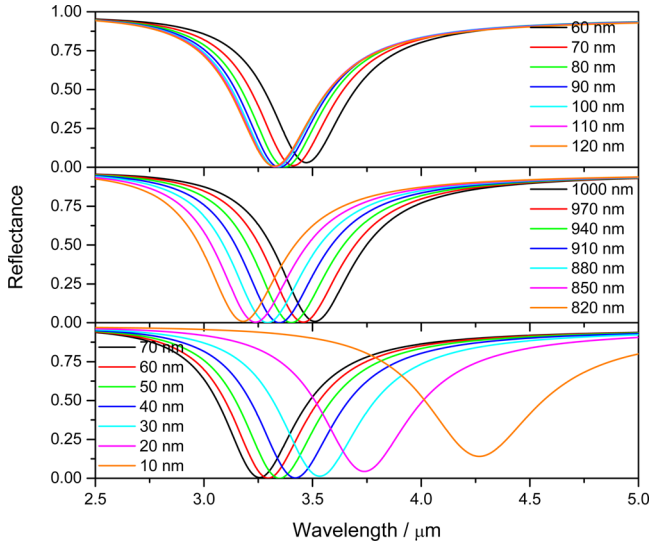

Figure 3. Dependence of the SPP wavelength on the slit parameters. Simulated reflectance spectra of the slit MPA for x-polarization. Shown are the influence of the variation of thickness of the Al_2O_3-layer (upper panel) of the period a (middle panel) and the slit width d (lower panel). The nonvaried parameters correspond to those from Figure 2.

The enhancement of the electric field E relative to the initial field E_0 at the resonance wavelength is depicted in Figure 4.

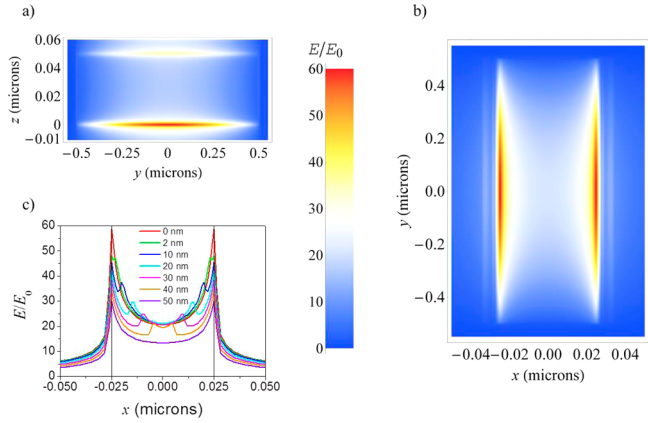

Figure 4. Electric field enhancement within the slit (same MPA as in Figure 2). (a) Electric field enhancement E/E_0 at a cross section within the slit 1 nm away from the slit wall (x = 0.024 μm). (b) Electric field enhancement E/E_0 at a cross section parallel to the surface of the substrate at the interface between Al_2O_3 and the second gold layer (z = 0 nm). (c) Electric field enhancement E/E_0 for y = 0 on the line where the enhancement is at the maximum, which is reached in the distance 0−1 nm away from the slit walls for different PE layer thicknesses. 10 nm, for example, means that both parts of the slit walls at the long sides that consist of gold (on the SiO_2 level the slits are unfilled) are covered with a 5 nm thick PE layer, leaving an empty slit with a width of 40 nm.

Accordingly, the enhancement is strongest one nm away from the slit walls within the slit along the long sides with a global maximum in the center of the long side. In the middle of the slit the amplification reaches a local minimum being lower for a completely filled slit than for an empty slit. Thus, even if the enhancement at first decreases with increasing z (see Figure 4a), it seems advisible to use the slit walls and functionalize them in order to bind and concentrate analytes in the

DOI: 10.1021/acsphotonics.5b00321
ACS Photonics 2015, 2, 1567−1575

neighbored volumes. Of course, if the slit walls are covered with analyte (in our simulations PE), the dielectric properties change the distribution of the enhancement (see Figure 4c). The thickness indicated in Figure 4c gives the sum of the (equal) thicknesses of the "left" and "right" layer, for example, "thickness 10 nm" means that the thickness of the left and right layer amount to 5 nm each. Correspondingly, 50 nm thickness means that both thicknesses amount to 25 nm, which translates into the slit being completely filled with PE at the level of the gold layer (at the level of the top SiO_2 layer the slit is always assumed to be empty). In this case, the enhancement decreases continually until the center is reached, whereas in the cases where the medium part of the slit is not filled, the interface between PE and empty slit is characterized by a sudden increase of the enhancement. From the results presented in Figure 4, we conclude that the SEIRA (surface enhanced infrared absorption; to be more precise, this slit array supports SEIRR, as it operates in reflection mode) slit array MPA is less prone to fabrication errors than particle based substrates as the slits show their maximum enhancement generally at sides, whereas particles based structures show the maximum enhancement at corners and fine structures due to the lightning rod effect.[21−28] It can be expected that such fine structures show a much stronger variance due to imperfect fabrication processes compared to edges of a slit. As a consequence, the deviations between different elementary cells can be expected to be much higher for particle based substrates than for slit-based substrates.

To determine how the spectral footprint changes with the thickness of the layers placed on the slit walls we performed different simulations the results of which are depicted in Figure 5. Even a thickness of 2 nm PE is easily detectable by a shift of the resonance band, whereas the spectral signature for this thickness is not easy to discern. Accordingly, the strengths of the slit MPA with this particular slit width d = 50 nm will be the detection of somewhat larger biomolecules, in particular, because of a reaction with capture molecules that are attached to the gold sidewalls.

Nonetheless, the sensitivity for the spectral fingerprint can be enlarged by decreasing the slit widths. As shown in Figure 5 (upper part), this shifts the main resonance to higher wavelengths but, nevertheless, increases the enhancement of the electric field strengths within the slit even for wavelengths comparably far away from the resonance range. This can be concluded from the comparison provided in the upper part of Figure 5, where the spectra of slits loaded with PE for slit widths from 70 nm down to 10 nm are shown. All spectra where calculated with a constant PE layer thickness of 5 nm at each long side, meaning that for the slit width 10 nm the slit is completely filled on the level of the gold sidewalls. Despite a strong redshift of the SPP resonance, which is, with 5.31 μm, far away from the vibrational resonances of PE due to the C−H stretching vibrations, the latter are easily detectable in the spectrum.

The comparison between the spectrum of the substrate with loaded and unloaded slits within an extended wavelength range is given in Figure 6. In addition to the spectral signature of the PE C−H stretching vibrations and an extraordinarily strong shift of the SPP resonance, even the spectral signature of the weak deformation vibration $\delta(CH_2)$ at 6.779 μm (1475 cm^{-1}, 1460−1470 cm^{-1} according to literature) can easily be detected. The corresponding spectral range is also of particular interest for biological sensing, as, in this range, the amide vibrational peaks of proteins, which show much higher vibrational intensities than $\delta(CH_2)$, can be found.[8] It is

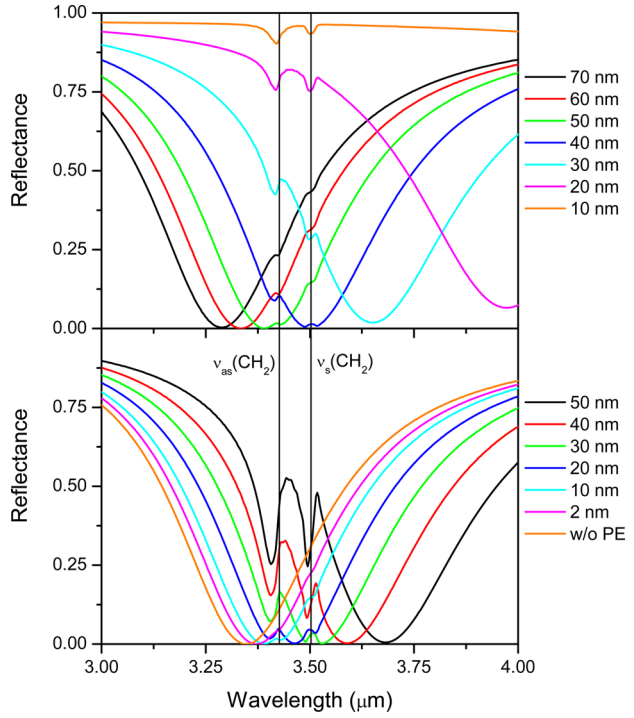

Figure 5. Simulated spectra of a subwavelength slit array metamaterial perfect absorber filled with analyte. Upper panel: influence of the slit width d on the normal incidence spectra when the PE layer thickness equals 10 nm. (For MPA with the smallest slit width this means that the slit is completely filled with PE on the level of the structured gold layer.) Lower panel: simulated reflectance spectra of a slit MPA with a = 1100 nm, b = 910 nm, c = 1000 nm, d = 50 nm, and $t_{Al_2O_3}$ = 90 nm for normal incidence in the spectral region of the main resonance. The panel displays spectra for an empty slit (orange) and a slit completely filled with PE (black), as well as for different layer thicknesses (cf. Figure 4c).

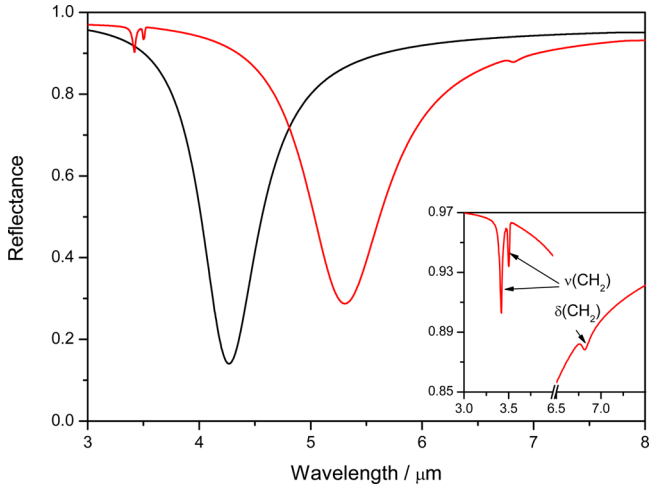

Figure 6. Simulated spectra of a subwavelength slit array metamaterial perfect absorber with 10 nm slit width. Simulated reflectance spectra of a slit MPA with a = 1100 nm, b = 910 nm, c = 1000 nm, d = 10 nm for normal incidence, and $t_{Al_2O_3}$ = 90 nm. Here we compared the x-polarized spectra of the slit MPA with empty slit (black) and slit filled with PE (red). The inset gives an enlargement of the regions with PE absorptions.

DOI: 10.1021/acsphotonics.5b00321
ACS Photonics 2015, 2, 1567−1575

remarkable that, for a slit width of 10 nm, the slit surface accounts only for about 1% of the whole area.

Nevertheless, the vast majority of the light passes through the slit at the wavelength of the resonance. (Note that we did not optimize the absorber for the slit width of 10 nm; virtually perfect absorption and an even better performance after optimization is likely.) The total volume of PE within the slit amounts to 1 μm × 0.05 μm × 0.01 μm. To clarify, under the assumption that the PE covers the total surface of the substrate, this would correspond to a layer of about 0.5 nm thickness (only a few C atoms thick). Even if small slit widths below 25 nm are hard to obtain from a technological point of view at the moment (yet may be accessible, e.g., by the use of photochemical metal deposition[17,18]), we are positive that this design will be valuable in the future once this limitation has been overcome. Since, despite its comparably narrow plasmon resonance, this slit perfect metamaterial absorber could be used not only for very sensitive refractive sensing, but also for enhancing most of the infrared spectral fingerprint of biomolecules with monolayer sensitivity, rendering it a highly desirable structure. In addition, the plasmon resonance is located in a spectral range between the stretching and bending vibrations of organic and biological molecules (between 3.5 and 5.5 μm). Therefore, strongly enhanced but nearly undistorted spectra can be gained.

To prove the simulation results, we fabricated a number of slit MPAs with dimensions close to the one the simulated spectra of which were presented in Figure 2 (a = 910 nm, b = 1100 nm, c = 1000 nm, d = 50 nm, and $t_{Al_2O_3}$ = 90 nm). We recorded IR spectra of the slit MPAs as fabricated as well as loaded with analytes showing C−H bands comparable to that of PE. A standard analyte, octadecanethiol (ODT), was used as a stand-in for PE due to their similarity with respect to the infrared spectral signatures and the ability of ODT to form chemically bound monolayers on gold surfaces that resist washing. The corresponding spectra, which were taken from substrate surfaces with an area of 1 mm^2 are presented in Figure 7a,b. Accordingly, the spectra represent averages of the spectral behavior of about 10^6 elementary cells and slits, respectively (spectral variances on the substrates are comparably small, cf. Figure S4 in the Supporting Information). The spectra show signal intensities of the C−H stretching vibrations and shifts of the plasmon bands that clearly exceed those which can be caused by an ODT monolayer based on the results of the simulations (cf. spectrum of a 2 nm thick PE layer in Figure 5, lower panel). This outcome is somewhat surprising yet gratifying as we used standard protocols which include washing steps to remove any ODT that is not covalently bound to the gold surface via its Sulfide-group (cf. Supporting Information, infrared spectroscopy).

We can only speculate that within the slits the van-der-Waals interaction between the hydrocarbon backbones is strong enough to withstand removal by the solvent even when not bound to the metal so that more ODT than expected remained in the slit. Free ODT should, in contrast to bound ODT, show bands according to the H−S-stretching vibrations (usually located between 3.85 and 4.16 μm). Unfortunately, these vibrations usually have comparably weak signal intensities, even when more thiol groups are present than in ODT. Therefore, it is not surprising that the corresponding bands cannot be seen in the spectra. We investigated the samples by SEM (Supporting Information, Figure S1), and the results support

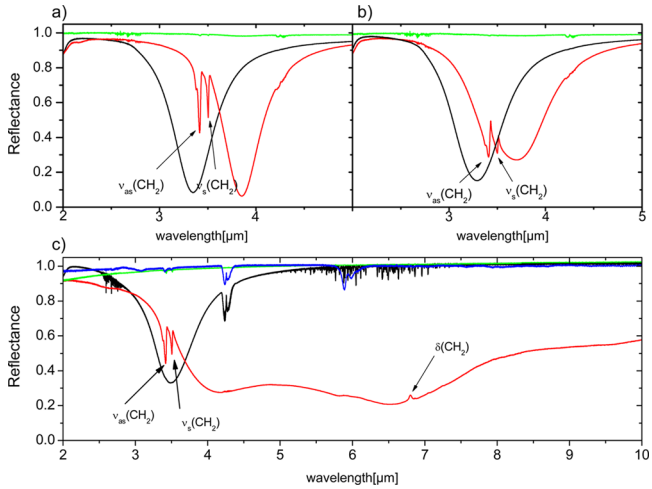

Figure 7. Experimental reflectance spectra of three slit MPAs at normal incidence (a = 910 nm, b = 1100 nm). (a) x-polarized spectra of a slit MPA (c = 974 nm, d = 40 nm, and $t_{Al_2O_3}$ = 90 nm) with empty slit (black) and after application of ODT, x-polarized (red) and y-polarized (green). (b) x-polarized spectra of a slit MPA (c = 993 nm, d = 50 nm, and $t_{Al_2O_3}$ = 90 nm) with empty slit (black) and after application of ODT, x-polarized (red) and y-polarized (green). (c) Spectrum of a slit MPA (c = 930 nm, d = 25 nm, and $t_{Al_2O_3}$ = 95 nm) before (black, y-polarized) and after application of a DNA/PBS mixture (red: y-polarized, green: x-polarized). Blue graph: Transmission spectrum of pure DNA.

the conclusion that the slits are partly filled by ODT. Even here the signal strengths are higher than expected on the basis of the simulation results (cf. Figure 5, lower part) since they exceed those for slits completely filled with PE. Yet, even if the analyte is not accumulated in the slits, the slit MPA outperforms competing plasmonic SEIRA substrate designs.[17,29−32] The probably most basic design consists of an array of gold nanowires ("nanoantennas") of about 1 μm lengths and being 0.1 μm diameter. In case of an end-to-end distance of the nanoantennas of 60 nm, the ODT signal in relative transmittance is about 1/3% of relative transmittance and increased to 1% if the end-to-end distance is decreased to 20 nm.[17] Very recently, the signal strength was improved even further. This was reached by placing the nanoantennae on a pedestal which allows the analyte to access to the region of highest enhancement more easily and increases the signal strength from 1 to 3%,[24] which is still an order of magnitude lower than the signal generated in our SHA-MPA combination. Another very recent approach is given by fan-shaped gold nanoantennas on a dielectric/gold layer sequence that also exploits the perfect absorber principle for SEIRA. As a consequence of the design, very high enhancements are reached, but most probably due to a disadvantageous average enhancement (only a very small area/volume of the substrate shows the strong enhancements), only a signal increase of the relative reflectance of 0.2% could be reached.[22] The signal strength is of the same order as the one also very recently reached by another perfect absorber based SEIRA substrate consisting of an array of nanoribbons.[32] Compared to such particle-based nanoantennas, our slit based approach has the additional and strong advantage that slits are much less prone to fabrication errors. The reason for this lies in the fact that the maximum field enhancement is not reached at a corner of the structure, the form of which usually shows variances from individual particle to particle, but at an edge

DOI: 10.1021/acsphotonics.5b00321
ACS Photonics 2015, 2, 1567−1575

(discussed above). This advantage is also exploited in ref 30, where nanogaps buried between two metals are used to generate SEIRA. Nevertheless, the signal in an albeit different analyte system (benzenethiol, peak at around 1475 cm^{-1}) does not exceed 0.2%. In general, we conclude that if design and accumulation are taken together, peak intensities for our SHA-MPA combination can be reached that exceed those of other SEIRA substrates by at least 1 order of magnitude.

As stated above, the slit is designed to also allow the detection of somewhat larger biomolecules. To prove this and since DNA contains a sugar−phosphate backbone, we decided to use it as a further model analyte to complete this study. As to be seen in Figure 7c, another at first unexpected enhancement of the C−H-bands (present due to the backbone-structure of DNA) occurs which goes hand in hand with an immensely broadened plasmon band. One explanation for this reproducible phenomenon would be that the crystallization of the salts in the PBS buffer (KH_2PO_4, NaCl, and KCl) used to incubate and dry the DNA strongly increases the real part of the dielectric function of the effective medium inside the slit. If this is the reason for the broadening of the plasmon band, this effect would prove highly convenient as it would make it possible to tune the plasmon resonance wavelength and width to match the analyte bands by adding different salts with different dielectric properties to the incubation solution. The small slope in the nonresonant polarization direction can be explained by PBS crystals still being present on the surface of the substrate (despite the washing step), which scatter and thus subdue part of the signal. This scattering should also change the signal for the resonant polarization direction, but the effect is superimposed by the plasmonic resonance and therefore not observable. The extraordinarily broad plasmon band leads to the fact that the weak deformation vibration $\delta(CH_2)$ band around 6.8 μm gets enhanced as well. The lack of N−H vibrations in the DNA/PBS spectrum of the MPA (which are present in the transmission spectrum of pure DNA, cf. Figure 7c) can be explained by the high content of thymine in the oligonucleotides used (and especially the part close to the gold surface), which has significantly less N−H than guanine, adenine, and cytosine.

Overall, we find that even with the slit widths d that can be achieved at the moment, our slit array metamaterial perfect absorber has the potential to outperform recent alternative approaches not only because of its mere performance, but also with respect to flexibility and potential. Through coating of less sensitive areas of the gold surface, the analyte is brought to selectively concentrate in the regions of highest enhancement. As a result, and in addition to refractive index sensing, our substrates provide a spectral fingerprint of analytes in the infrared spectral region strong enough to easily detect them via standard lab equipment. Most probably, the signals can be further enhanced and tuned by the addition of salts that crystallize in the slits. The crystallization strongly broadens the plasmon resonance so that the enhancement covers a large spectral region of the Mid-IR. Moreover, once smaller slits widths around 10 nm are technologically possible, the plasmon resonance can be shifted to the uninteresting spectral region between the stretching and deformation vibrations of the analytes. (N.B.: This also breaks the paradigm that the existence of a Fano-type interaction is a necessary prerequisite for surface-enhanced infrared spectroscopy!) As a consequence, the spectral fingerprints of the analytes would no longer be disturbed, while the stronger enhancement leads to the coverage of the whole spectral region of interest. All in all, the slit array metamaterial perfect absorber has great potential as a future substitute for sensors based on the conventional excitation of surface plasmon resonances. To substitute conventional sensors is of particular interest in point-of-care analysis, due to the challenging needs for chemical sensitivity and less complex as well as more compact detection units.

METHODS

Numerical Modeling. The numerical modeling was carried out with the finite-difference time-domain (FDTD) method, as implemented in the software "FDTD solutions" from Lumerical. The FDTD method is a well-established technique to simulate the optical response of nanostructured materials.[33] It is based on the time-dependent Maxwell equations in partial differential form. To solve these, both space and time are discretized. The differentials are then estimated using central-difference approximations. The resulting equations are solved iteratively until a steady state behavior is reached. The convergence of the solutions to the exact solutions of the Maxwell equations depends on a suitable choice of the number of discretization steps and the simulation time. For our simulation, we validated convergence by letting selected simulations run with stronger discretization and longer simulation times. Selected simulations were cross-checked by modeling the structure again with the finite element method (FEM). Generally, we enforced stronger discretization within the slit and in the dielectric layer below the slit (Δx = 1 nm, Δy = 5 nm, Δz = 2 nm, where x is oriented parallel to the slit width, y to the length, and z to the depth). The residual structure was covered with an automatically generated grid by choosing Lumerical's "high accuracy" inbuilt standard process. Due to the rectangular design of our SHA-MPA, we could also force the interfaces of the structures to coincide with the mesh. The total modeling volume was 810−1000 nm (period in x) by 1100 nm (period in y) by 11 μm (z-direction; direction of the incoming light). To reduce calculation times, symmetry was exploited and periodic boundary conditions were applied at the x- and y-boundaries. The z-boundaries were surrounded by perfectly matched layers. For the gold layers, we used optical constants based on Johnson and Christy[19] in parametrized form, as suggested by Etchegoin et al.,[34,35] since these allowed for an overall better prediction of the experimental data than recent results for dielectric functions measured directly in the MIR[36,37] (as a trade-off between full width at half minimum, position and value at minimum, cf. Supporting Information, Figure S2), SiO_2 and Al_2O_3 layers were modeled with built-in data from Palik.[20] Polyethylene (PE) was chosen as an organic analyte primarily since its optical constants in the infrared have been determined[38] and the bands in the spectral region of interest resemble those of one of the model analytes, namely, octadecanethiol[17] and, to some extent, DNA.

Fabrication. To prepare the SHA-MPA gratings, we started with prefabricated Si chips (size 15 × 15 mm^2), which contain six numbered gold mirror plates with a size of 2 × 2 mm^2 and a gold thickness of 50 nm.[39]

Several chips were individually coated with thin Al_2O_3 spacer films of different thicknesses $t_{Al_2O_3}$ (90, 95, and 100 nm), precisely fabricated by using atomic layer deposition (ALD) followed by the evaporation of a 50 nm thick gold layer. The gold layer was covered with a 10 nm thick SiO_2 top layer. The plasma-enhanced ALD process was performed with an OpAL-

DOI: 10.1021/acsphotonics.5b00321
ACS Photonics 2015, 2, 1567−1575

reactor from Oxford Instruments (upgraded with an inductive-coupled plasma source). As precursors in the ALD processes, we used trimethylaluminum (TMAl) for aluminum oxide (Al_2O_3) and tris(dimethylamino)-silane (TDMAS) for silicon oxide (SiO_2). Al_2O_3 was deposited with thermal ALD, using water as second precursor. The deposition temperature was 120 °C. SiO_2 was deposited with remote oxygen plasma at a plasma pressure of 22.3 Pa. The growth rate of SiO_2 was estimated to 1.19 ± 0.06 Å/cycle, the rate of thermally deposited Al_2O_3 was 1.05 ± 0.06 Å/cycle.

The nanometer-scale slit patterns of the SHA-MPA gratings were made by shaped electron beam lithography and Ar^+-ion beam etching. As electron beam resist the AR6200.09 from Allresist GmbH Berlin was used. The resist was spun to a thickness of 155 nm and was additionally covered with a 10 nm thick gold conduction layer made by thermal evaporation. The e-beam exposure of the six SHA-MPA gratings per chip (each with a size of 1 × 1 mm^2) was performed using the shaped e-beam writer SB350 OS (50 keV, Vistec Electron Beam GmbH) at an electron dose of 400 $\mu C/cm^2$. Employing this tool, the exposure time per grating was only 2.5 min.[40] The resist was developed for 60 s in AR600−546 (Allresist) and rinsed for 30 s in isopropanol (IPA). After the ion beam etching (60 s, 400 eV, 150 W, 0.5 mA/cm^2), the resist mask was removed and the surface cleaned by using an O_2-plasma treatment (1 min, 50 W). Afterward, samples were polished with an angled ion-beam polishing to remove sidewall redeposition.

Depending on the layout size and the electron dose, SHA-MPA gratings with slit widths from 25 to 80 nm and slit lengths from 930 to 1000 nm were fabricated with a pitch of 910 nm in x-direction and 1100 nm in y-direction.

Infrared Spectroscopy. The IR reflection spectra were recorded with a Bruker Vertex 80v FT-spectrometer with an attached IR Microscope (HYPERION 2000) featuring a 15× − Cassegrain IR objective with 0.4 NA. The experiments were conducted with a resolution of 0.5 to 1 cm^{-1}. To polarize the incidence beam a KRS-5 polarizer was used with a spectral window from 7500 to 370 cm^{-1}. As detector, a LN-MCT detector from Bruker was employed (MCT-D316). Reflection measurements were referenced against Au mirrors. To minimize influence of ambient air, the spectrometer compartment was evacuated below 3 mbar and the microscope body and purge box were flushed with N_2. Record mode was single-sided forward−backward sampling with Mertz and Blackman-Harris 3-term chosen for phase correction and apodization, respectively. As default, 64 spectra were averaged.

As samples were used octadecanethiol (Sigma-Aldrich, 98% purity) as well as SS150DNA oligonucleotides featuring a thiol group. In the case of octadecanethiol, the substrate was O_2-plasma cleaned to remove any adhered organic contaminants to the surface before immersing the samples in 20 μL of 1:10 diluted saturated ODT + ethanol solution. After 40 min, the chips were cleaned with rinsing in running EtOH (4 s) before submersing in pure EtOH for 40 min. Drying was done by pressurized N_2 (5 s, until EtOH was completely evaporated).

For DNA measurements, DNA (100 μmolar concentration; TTTTTTCAGCATGTGCTCCTTGATTCTATG with thiol group, from Eurofins) was diluted 1:10 in 5× PBS buffer and the chip was covered with 20 μL of solution left to dry overnight (15 h), resulting in filled slits. Subsequently, the chips were rinsed for 20 s in deionized water to remove salt crystals formed by the PBS on the surface before drying in nitrogen gas and measurement.

Fluorescence Spectroscopy. For fluorescence imaging an ELYRA SIM (structured illumination microscope) was used with 488 nm laser excitation and a 520 nm filter for fluorescence light. The fluorophore (SAMSA fluoresceine A-685 from life-technologies) was sensitive at 495 nm and emission wavelength was 520 nm. The thiol group contained in this fluorophore was activated as by the manufacturer's instructions and drop-dried on the structure. Afterward, the chips were rinsed to remove nonbound fluorophore. Samples were then immersed in index-matching oil, covered with a cover slide and topped with more oil to prevent contamination. A 63× objective with 1.4 NA was used to record the images shown in Figure 1. Data processing was automatically done by the Zen Software for the ELYRA microscope. Afterward, a Fourier-transformation was performed, giving an indication of the bridges between the slits in y-direction by showing a periodic signal. To avoid negative effects by of the oil used, other samples were also examined on a standard fluorescence microscope with 100× objective (0.9 NA) made by Zeiss.

■ ASSOCIATED CONTENT

Supporting Information

The Supporting Information is available free of charge on the ACS Publications website at DOI: 10.1021/acsphotonics.5b00321.

Tuning of resonance wavelength, figure of merit, influence of the dielectric function of gold (PDF).

Movie S1. Simulated electric field changes of a slit MPA with a = 910 nm, b = 1100 nm, c = 1000 nm, d = 50 nm and $t_{Al_2O_3}$ = 90 nm (x-polarized, slit empty) in the spectral range of the main resonance (light pulse duration: 500 fs, center wavelength 3.35 μm, overall length of the simulation: 1500 fs). a) View direction along −z, visible plane at z = 0 (interface between Al_2O_3-layer and structured gold layer) (AVI). b) View direction along y-axis, visible plane at y = 0 (center of the slit) (AVI) c) View direction along x-axis, visible plane at x = 0 (center of the slit) (AVI)

Movie S2. Simulated electric field changes of a slit MPA with a = 910 nm, b = 1100 nm, c = 1000 nm, d = 50 nm and $t_{Al_2O_3}$ = 90 nm (y-polarized, slit empty) in the spectral range of the main resonance (light pulse duration: 500 fs, center wavelength 3.35 μm, overall length of the simulation: 1500 fs). a) View direction along −z, visible plane at z = 0 (interface between Al_2O_3-layer and structured gold layer) (AVI) b) View direction along y-axis, visible plane at y = 0 (center of the slit) (AVI) c) View direction along x-axis, visible plane at x = 0 (center of the slit) (AVI).

Movie S3. Simulated electric field changes of a slit MPA with a = 910 nm, b = 1100 nm, c = 1000 nm, d = 50 nm and $t_{Al_2O_3}$ (x-polarized, slit empty) in the spectral range of the main resonance (light pulse duration: 500 fs, center wavelength 6 μm, overall length of the simulation: 1500 fs). a) View direction along −z, visible plane at z = 0 (interface between Al_2O_3-layer and structured gold layer) (AVI) b) View direction along y-axis, visible plane at y = 0 (center of the slit) (AVI) c) View direction along x-axis, visible plane at x = 0 (center of the slit) (AVI).

DOI: 10.1021/acsphotonics.5b00321
ACS Photonics 2015, 2, 1567−1575

AUTHOR INFORMATION

Corresponding Author

*E-mail: thomas.mayerhoefer@ipht-jena.de.

Notes

The authors declare no competing financial interest.

ACKNOWLEDGMENTS

Funding of the research projects "Jenaer Biochip Initiative 2.0" (03IPT513Y) within the framework "Unternehmen Region − InnoProfile Transfer" supported by the Federal Ministry of Education and Research, Germany (BMBF) and "PhoNa - Photonic Nanomaterials" (03IS2101A) supported by the German Federal Ministry of Education and by the Thuringian Ministry for Education, Science, and Culture is gratefully acknowledged. For the recording of the SIM-FLOUR image, we are deeply grateful to Martin Kielhorn and Rainer Heintzmann. For assistance in the preparation of the substrate, we are much obliged to the following colleagues: Hermann Roth (e-beam), Katrin Pippardt (resist and lithography), Birger Steinbach (evaporation), Katrin Kandera (ion beam etching), and Mario Ziegler (ALD).

REFERENCES

(1) Watts, C. M.; Liu, X.; Padilla, W. J. Metamaterial electromagnetic wave absorbers. *Adv. Mater.* **2012**, *24*, 98−120.

(2) Liu, N.; Mesch, M.; Weiss, T.; Hentschel, M.; Giessen, H. Infrared perfect absorber and its application as plasmonic sensor. *Nano Lett.* **2010**, *10*, 2342−8.

(3) Song, Y.; Wang, C.; Lou, Y.; Cao, B.; Li, X. Near-perfect absorber with ultrawide bandwidth in infrared region using a periodically chirped structure. *Opt. Commun.* **2013**, *305*, 212−216.

(4) Wu, C.; Shvets, G. Design of metamaterial surfaces with broadband absorbance. *Opt. Lett.* **2012**, *37*, 308−310.

(5) Hendrickson, J.; Guo, J. P.; Zhang, B. Y.; Buchwald, W.; Soref, R. Wideband perfect light absorber at midwave infrared using multiplexed metal structures. *Opt. Lett.* **2012**, *37*, 371−373.

(6) Bouchon, P.; Koechlin, C.; Pardo, F.; Haidar, R.; Pelouard, J. L. Wideband omnidirectional infrared absorber with a patchwork of plasmonic nanoantennas. *Opt. Lett.* **2012**, *37*, 1038−40.

(7) Liu, Y.; Gu, S.; Luo, C.; Zhao, X. Ultra-thin broadband metamaterial absorber. *Appl. Phys. A: Mater. Sci. Process.* **2012**, *108*, 19−24.

(8) Li, Y.; Su, L.; Shou, C.; Yu, C.; Deng, J.; Fang, Y. Surface-enhanced molecular spectroscopy (SEMS) based on perfect-absorber metamaterials in the mid-infrared. *Sci. Rep.* **2013**, *3*, 2865.

(9) Grant, J.; Ma, Y.; Saha, S.; Khalid, A.; Cumming, D. R. Polarization insensitive, broadband terahertz metamaterial absorber. *Opt. Lett.* **2011**, *36*, 3476−8.

(10) Aydin, K.; Ferry, V. E.; Briggs, R. M.; Atwater, H. A. Broadband polarization-independent resonant light absorption using ultrathin plasmonic super absorbers. *Nat. Commun.* **2011**, *2*, 517.

(11) Feng, R.; Ding, W.; Liu, L.; Chen, L.; Qiu, J.; Chen, G. Dual-band infrared perfect absorber based on asymmetric T-shaped plasmonic array. *Opt. Express* **2014**, *22*, A335.

(12) Xiong, X.; Xue, Z.-H.; Meng, C.; Jiang, S.-C.; Hu, Y.-H.; Peng, R.-W.; Wang, M., Polarization-dependent perfect absorbers/reflectors based on a three-dimensional metamaterial. *Phys. Rev. B: Condens. Matter Mater. Phys.* **2013**, *88*.10.1103/PhysRevB.88.115105

(13) Hu, C.; Zhao, Z.; Chen, X.; Luo, X. Realizing near-perfect absorption at visible frequencies. *Opt. Express* **2009**, *17*, 11039−11044.

(14) Fang, Z.; Zhen, Y.-R.; Fan, L.; Zhu, X.; Nordlander, P., Tunable wide-angle plasmonic perfect absorber at visible frequencies. *Phys. Rev. B: Condens. Matter Mater. Phys.* **2012**, *85*.10.1103/PhysRevB.85.245401

(15) Limaj, O.; D'Apuzzo, F.; Di Gaspare, A.; Giliberti, V.; Domenici, F.; Sennato, S.; Bordi, F.; Lupi, S.; Ortolani, M. Mid-Infrared Surface Plasmon Polariton Sensors Resonant with the Vibrational Modes of Phospholipid Layers. *J. Phys. Chem. C* **2013**, *117*, 19119−19126.

(16) Weber, D.; Albella, P.; Alonso-Gonzalez, P.; Neubrech, F.; Gui, H.; Nagao, T.; Hillenbrand, R.; Aizpurua, J.; Pucci, A. Longitudinal and transverse coupling in infrared gold nanoantenna arrays: long range versus short range interaction regimes. *Opt. Express* **2011**, *19*, 15047−15061.

(17) Pucci, A.; Neubrech, F.; Weber, D.; Hong, S.; Toury, T.; de la Chapelle, M. L. Surface enhanced infrared spectroscopy using gold nanoantennas. *Phys. Status Solidi B* **2010**, *247*, 2071−2074.

(18) Neubrech, F.; Weber, D.; Katzmann, J.; Huck, C.; Toma, A.; Di Fabrizio, E.; Pucci, A.; Hartling, T. Infrared optical properties of nanoantenna dimers with photochemically narrowed gaps in the 5 nm regime. *ACS Nano* **2012**, *6*, 7326−32.

(19) Johnson, P. B.; Christy, R. W. Optical Constants of the Noble Metals. *Phys. Rev. B* **1972**, *6*, 4370−4379.

(20) Palik, E. D. *Handbook of Optical Constants of Solids, Five-Vol. Set: Handbook of Thermo-Optic Coefficients of Optical Materials with Applications*; Elsevier Science: New York, 1997.

(21) Adato, R.; Altug, H. In-situ ultra-sensitive infrared absorption spectroscopy of biomolecule interactions in real time with plasmonic nanoantennas. *Nat. Commun.* **2013**, *4*, 2154.

(22) Aksu, S.; Cetin, A. E.; Adato, R.; Altug, H. Plasmonically Enhanced Vibrational Biospectroscopy Using Low-Cost Infrared Antenna Arrays by Nanostencil Lithography. *Adv. Opt. Mater.* **2013**, *1*, 798−803.

(23) Bochterle, J.; Neubrech, F.; Nagao, T.; Pucci, A. Angstrom-Scale Distance Dependence of Antenna-Enhanced Vibrational Signals. *ACS Nano* **2012**, *6*, 10917−10923.

(24) Brown, L. V.; Zhao, K.; King, N.; Sobhani, H.; Nordlander, P.; Halas, N. J. Surface-enhanced infrared absorption using individual cross antennas tailored to chemical moieties. *J. Am. Chem. Soc.* **2013**, *135*, 3688−95.

(25) Huck, C.; Neubrech, F.; Vogt, J.; Toma, A.; Gerbert, D.; Katzmann, J.; Härtling, T.; Pucci, A. Surface-Enhanced Infrared Spectroscopy Using Nanometer-Sized Gaps. *ACS Nano* **2014**, *8*, 4908−4914.

(26) Kusa, F.; Ashihara, S., Spectral response of localized surface plasmon in resonance with mid-infrared light. *J. Appl. Phys.* **2014**, *116*.15310310.1063/1.4898316

(27) Liberman, V.; Adato, R.; Mertiri, A.; Yanik, A. A.; Chen, K.; Jeys, T. H.; Erramilli, S.; Altug, H. Angle-and polarization-dependent collective excitation of plasmonic nanoarrays for surface enhanced infrared spectroscopy. *Opt. Express* **2011**, *19*, 11202−11212.

(28) Neubrech, F.; Beck, S.; Glaser, T.; Hentschel, M.; Giessen, H.; Pucci, A. Spatial Extent of Plasmonic Enhancement of Vibrational Signals in the Infrared. *ACS Nano* **2014**, *8*, 6250−6258.

(29) Brown, L. V.; Yang, X.; Zhao, K.; Zheng, B. Y.; Nordlander, P.; Halas, N. J. Fan-Shaped Gold Nanoantennas above Reflective Substrates for Surface-Enhanced Infrared Absorption (SEIRA). *Nano Lett.* **2015**, *15*, 1272−80.

(30) Chen, X.; Ciraci, C.; Smith, D. R.; Oh, S. H. Nanogap-enhanced infrared spectroscopy with template-stripped wafer-scale arrays of buried plasmonic cavities. *Nano Lett.* **2015**, *15*, 107−13.

(31) Huck, C.; Toma, A.; Neubrech, F.; Chirumamilla, M.; Vogt, J.; De Angelis, F.; Pucci, A. Gold Nanoantennas on a Pedestal for Plasmonic Enhancement in the Infrared. *ACS Photonics* **2015**, *2*, 497−505.

(32) Ishikawa, A.; Tanaka, T. Metamaterial Absorbers for Infrared Detection of Molecular Self-Assembled Monolayers. *Sci. Rep.* **2015**, *5*, 12570.

(33) Bondeson, A.; Rylander, T.; Ingelström, P. *Computational Electromagnetics*; Springer: New York, 2005.

(34) Etchegoin, P. G.; Le Ru, E. C.; Meyer, M. An analytic model for the optical properties of gold. *J. Chem. Phys.* **2006**, *125*, 164705.

(35) Etchegoin, P. G.; Le Ru, E. C.; Meyer, M. Erratum: "An analytic model for the optical properties of gold. *J. Chem. Phys.* **2006**, *125*, 164705; *J. Chem. Phys.* **2007**, *127*, 189901.

DOI: 10.1021/acsphotonics.5b00321
ACS Photonics 2015, 2, 1567−1575

(36) Olmon, R. L.; Slovick, B.; Johnson, T. W.; Shelton, D.; Oh, S. H.; Boreman, G. D.; Raschke, M. B., Optical dielectric function of gold. *Phys. Rev. B: Condens. Matter Mater. Phys.* **2012**, *86*.10.1103/PhysRevB.86.235147

(37) Trollmann, J.; Pucci, A. Infrared Dielectric Function of Gold Films in Relation to Their Morphology. *J. Phys. Chem. C* **2014**, *118*, 15011−15018.

(38) Zolotarev, V. M.; Volchek, B. Z.; Vlasova, E. N. Optical constants of industrial polymers in the IR region. *Opt. Spectrosc.* **2006**, *101*, 716−723.

(39) Huebner, U.; Pshenay-Severin, E.; Alaee, R.; Menzel, C.; Ziegler, M.; Rockstuhl, C.; Lederer, F.; Pertsch, T.; Meyer, H.-G.; Popp, J. Exploiting extreme coupling to realize a metamaterial perfect absorber. *Microelectron. Eng.* **2013**, *111*, 110−113.

(40) Huebner, U.; Falkner, M.; Zeitner, U. D.; Banasch, M.; Dietrich, K.; Kley, E.-B. Multi-stencil character projection e-beam lithography: a fast and flexible way for high quality optical metamaterials. 30th European Mask and Lithography Conference, Dresden, Germany, June 24, 2014, SPIE: Bellingham WA, 20149231; 10.1117/12.2065944

DOI: 10.1021/acsphotonics.5b00321
ACS Photonics 2015, 2, 1567−1575